

Virgo High-Resolution CO Survey: IV. Spiral-Driven Gas Dynamics in the Non-Barred Seyfert Galaxy NGC 4501

Sachiko ONODERA,¹ Jin KODA,^{1,2,3} Yoshiaki SOFUE,¹ and Kotaro KOHNO¹

¹*Institute of Astronomy, The University of Tokyo, Mitaka, Tokyo 181-0015*

²*Nobeyama Radio Observatory, National Astronomical Observatory, Minamimaki, Minamisaku, Nagano 384-1305*

³*ALMA Project Office, National Astronomical Observatory, Mitaka, Tokyo 181-8588*

sonodera@ioa.s.u-tokyo.ac.jp

(Received 2003 October 28; accepted 2004 April 21)

Abstract

We report on high-resolution interferometer observations of the ^{12}CO ($J = 1-0$) emission in the central 5 kpc region of the Seyfert 2 galaxy NGC 4501. The observations were made using the Nobeyama Millimeter Array during a long-term CO line survey of Virgo spirals. The major features are: (1) a nuclear concentration with a radius of $r \sim 5''$ (390 pc), which is resolved into double peaks, and (2) spiral arms which extend out from the nuclear region. The nuclear component has a mass of $1.3 \times 10^8 M_{\odot}$, which corresponds to $\sim 3.5\%$ of the dynamical mass, and shows a slight non-circular motion. The double peaks are separated by $\sim 4.''7$ (370 pc), and located on the root of optical spiral arms in a HST image. The gas arms are associated with the spiral dust lanes, and are linked to the central double peaks. The non-circular motions along the molecular arms indicate the fact that the gas is driven by the density wave, rather than the stochastic processes. We calculated the gas cloud orbits in a stellar spiral potential, and explained the observed CO spiral arms and non-circular motions. We suggest that the central gas condensation arises from spiral-driven gas transfer. We estimated and compared the effect of two possible mechanisms of angular-momentum transfer: galactic shock and gravitational torques. We discuss that the galactic shock is dominant.

Key words: galaxies: individual (NGC 4501) — galaxies: ISM — galaxies: kinematics and dynamics — galaxies: Seyfert — galaxies: spiral

1. Introduction

Gas dynamics in disk galaxies is closely related to the stellar potential. Gas dynamics in barred galaxies has been well studied in particular, and many observed features have been successfully explained. Bars are thought to be the most viable candidates for fueling the central activity, transferring mass from large to small scales (e.g. Simkin et al. 1980; Shlosman et al. 1989; Athanassoula 1992). Recent statistics report circumstantial evidence of radial gas inflow as a result of bar-driven gas dynamics. Metallicity gradients in barred spirals are systematically flatter than that of unbarred ones, and they become shallower when the bar length and the bar ellipticity increase (Martin, Roy 1994). The degree of gas condensation to the central kiloparsec is higher in barred galaxies than in unbarred ones (Sakamoto et al. 1999b).

However, the central gas condensation is also prevalent in non-barred galaxies (Sakamoto et al. 1999a), and some studies claim that the level of the central activity does not correlate with the presence of large-scale bars (Ho et al. 1997b; Mulchaey, Regan 1997). Their results suggest that gas inflow may occur both in barred and non-barred spiral galaxies. Although a theoretical study of the gas dynamics in spiral galaxies with tightly wound arms was in full flourish several decades ago (e.g. Fujimoto 1968b; Roberts 1969), its application for observational data and discussions within the context of radial mass transfer has not been thoroughly pursued compared to that in barred galaxies.

We observed a non-barred CO-luminous galaxy, NGC 4501,

during the Virgo high-resolution CO survey (ViCS: Sofue et al. 2003), using the Nobeyama Millimeter Array with the highest resolution ever achieved for this galaxy. The prominent molecular arm structure, non-circular motion, and centrally-condensed double peaks motivated our work on the gas dynamics in the spiral potential and possible inflow mechanism to the center.

NGC 4501 is one of some non-barred galaxies that have a relatively high degree of central gas condensation, similar to those of barred galaxies (Sakamoto et al. 1999b). It is an SAB galaxy (de Vaucouleurs et al. 1991, hereafter RC3) at a distance of 16.1 Mpc (Ferrarese et al. 1996; $1''$ corresponds to 78 pc) located about $2.^{\circ}0$ (0.56 Mpc) northeast of the center of the Virgo cluster, M 87. It hosts a weak Seyfert 2 nucleus (Ho et al. 1997a). It is slightly H I deficient (Chamaraux et al. 1980), and has a high CO luminosity and a high IRAS flux density (Stark et al. 1986). While it is not classified as a grand-design spiral galaxy in B -band image (arm class 9; Elmegreen, Elmegreen 1987), it shows continuous two-armed spiral in the K' -band within $r \lesssim 3$ kpc (Elmegreen et al. 1999, see their figure 1). Moreover, Carollo et al. (1998) noted the spiral-like dust lanes down to the nucleus in the F606W (wide V -band) image of HST WFPC2. The basic properties of NGC 4501 are listed in table 1.

In this paper, we show that the gas dynamics in the central region of this galaxy is governed by a stellar spiral potential, and suggest the possibility that the observed central features can be the outcome of radial inflow due to the spiral arms. High-resolution ^{12}CO ($J = 1-0$) observations of NGC 4501 are

Table 1. Parameters of NGC 4501.

Parameter	Value	Source*
Hubble type	SA(rs)b	1
Nuclear activity	Type 2 Seyfert	2
Adopted distance (Mpc)	16.1	3
P.A. (isophotal) ($^{\circ}$)	140	4
Inclination ($^{\circ}$)	58	4
$D_{25} \times d_{25}$	6.9×3.7	1
V_{sys} (km s^{-1})	2263	4
B_{total}^0 (mag)	9.86	1
$S_{\text{CO}}(45'')$ (K km s^{-1})	12.0 ± 4	4
Linear scale (pc arcsec^{-1})	78.1	

* (1) de Vaucouleurs et al. (1991) (RC3); (2) Ho et al. (1997a);
(3) Ferrarese et al. (1996); (4) Kenney and Young (1988).

Table 2. Observation parameters

Observed center frequency (GHz)	114.407
Array configurations	AB, C, and D
Observing field center (Sakamoto et al. 1999a):	
α (J2000)	$12^{\text{h}}31^{\text{m}}59^{\text{s}}.14$
δ (J2000)	$+14^{\circ}25'12''.9$
Frequency channels	256
Total bandwidth (MHz)	512
Velocity coverage (km s^{-1})	1342
Velocity resolution (km s^{-1})	5.24
Amplitude and phase calibrator	3C 273
Primary beam ($''$)	65

presented in section 2. The results from the observations are presented in section 3. The CO distribution and the velocity field are modeled based on observations in section 4. Possible mechanisms of spiral-induced radial gas inflow are discussed in section 5. We summarize our conclusions in section 6. A detailed description of the damped-orbit model in the spiral potential is shown in appendix 1. An estimation of the change in the angular momentum with shocks and torques is presented in appendix 2.

2. Observations and Reduction

2.1. CO ($J = 1-0$) Observations with NMA

We carried out observations of NGC 4501 in the ^{12}CO ($J = 1-0$) line using the Nobeyama Millimeter Array (NMA) at the Nobeyama Radio Observatory (NRO) during the course of a long-term project, the Virgo high-resolution CO Survey (ViCS; Sofue et al. 2003). The observations were made from 2000 December to 2002 March for a single pointing center at $(\alpha_{\text{J2000}}, \delta_{\text{J2000}}) = (12^{\text{h}}31^{\text{m}}59^{\text{s}}.14, +14^{\circ}25'12''.9)$. The NMA consisted of six antennas, each had a diameter of 10 m, providing a FWHP of about $65''$ at 115 GHz. We used the spectro-correlator Ultra-Wide-Band Correlator (UWBC; Okumura et al. 2000), in a mode of 256 channels covering 512 MHz. One channel (2 MHz) corresponded to 5.2 km s^{-1} at the observing frequency. Quasar 3C 273 was observed every 20 minutes to correct for any instrumental gain variations and the bandpass response. Continuum observations of Mars were used to calibrate the flux scale. We calibrated the absolute flux scale in each sideband in each observation: once in 2000, three times in 2001, and once in 2002. We compared the noises in two sidebands and used the lower sideband (102 GHz) data in all flux calibrations. The flux density of 3C 273 was roughly constant at 9.6 Jy , within $\pm \sim 20\%$. No significant flux variation was observed in all of our runs. The chopper-wheel method was used to correct for any atmospheric transmission losses and elevation-dependent gain variations. We used AB, C, and D array configurations of the NMA to achieve a resolution of less than $2''$. The visibility data cover projected baselines from 10 to 341 m. Partially shadowed observation data were deleted, and the minimum baseline length projected

onto the sky was the diameter of each antenna. This resulted in the central hole in the $u-v$ plane, which restricts the largest detectable size of objects to about $54''$. The observation parameters are listed in table 2.

2.2. Reduction

The raw visibility data were calibrated with the NRO/UVPROC2 software (Tsumumi et al. 1997) and mapped with the NRAO/AIPS package. We applied the CLEAN procedure with two ways of weighting (natural and pure uniform), and obtained three-dimensional data cubes (R.A., Decl., V_{LSR}) in low ($5''$) and high ($2''$) spatial resolutions. The synthesized beam parameters, velocity resolutions, and rms noises for these maps are listed in table 3. The fraction of the total flux recovered by our NMA data cube was estimated by comparing with single-dish observations using the FCRAO 14 m telescopes (Kenney, Young 1988). For this comparison, the data cube was corrected for the primary beam attenuation of the NMA antennas, convolved with the single-dish beam (FCRAO, $45''$), and sampled at the pointing centers of the single-dish observations to obtain a value comparable to the single-dish flux. The NMA cube was found to recover about 78% of the single-dish flux in the central $45''$. Note, however, the primary beam correction was not applied to the maps shown in this paper.

Figures 1 and 2 display low- and high-resolution integrated intensity maps and velocity fields in the central region of NGC 4501 ($90'' \sim 7.0 \text{ kpc}$ square for figure 1, $14'' \sim 1.1 \text{ kpc}$ for figure 2). The crosses in figure 1 and figure 2 indicate the major and minor axes of NGC 4501 (P.A. = 140°). The ellipse in figure 1 indicate a projected circle of diameter $75''$ (5.9 kpc), inclined with the position angle and inclination (58°) of this galaxy. The size of the crosses in high-resolution maps is $5''$ (390 pc). The center of all crosses and ellipses in figures 1 and 2 are set at the dynamical center derived from the velocity field (see below).

Figure 3 shows channel maps with an interval of 4 MHz (10.4 km s^{-1}) in the same region. Significant emission ($> 3\sigma$, $1\sigma = 14 \text{ mJy beam}^{-1}$) was detected in 46 adjacent channels within the velocity range of $V_{\text{LSR}} = 2044-2513 \text{ km s}^{-1}$ ($\Delta V = 269 \text{ km s}^{-1}$). In order to check the contribution of the continuum flux, we examined the lower sideband (102 GHz) data that can be regarded as being emission-free. We summed

Table 3. Parameters of maps.*

Resolution	Weighting	Beam		Velocity resolution (km s^{-1})	rms noise σ (mJy beam^{-1})	T_b for 1 Jy beam^{-1} (K)
		FWHM ($''$)	P.A. ($^\circ$)			
Low	Natural	5.6×3.7	160	10.5	14	4.5
High	Pure uniform	1.8×1.7	138	41.9	16	30.5

* The map centers are set at derived dynamical center: $(\alpha_{J2000}, \delta_{J2000}) = (12^{\text{h}}31^{\text{m}}59^{\text{s}}.12, +14^{\circ}25'13''.3)$ and derived systemic velocity 2261 km s^{-1} .

up our data over the full bandwidth (512 MHz); no significant continuum flux ($> 3\sigma$, $1\sigma = 1.3 \text{ mJy beam}^{-1}$) was detected.

We obtained kinematical parameters from the low-resolution ($5''$) velocity field using the AIPS/GAL package. The dynamical center (table 2) was determined using the Brandt rotation curve model (Brandt, Scheer 1965). For fitting, we used the central $r < 5''$ region where the velocity field can be regarded as being nearly symmetric against the dynamical center. The initial guess of the parameters affected the result within $r < 1''$. The centers of CO maps and PV diagram are set at this derived dynamical center: $(\alpha_{J2000}, \delta_{J2000}) = (12^{\text{h}}31^{\text{m}}59^{\text{s}}.12, +14^{\circ}25'13''.3)$ and the systemic velocity $V_{\text{sys}} = 2261 \text{ km s}^{-1}$. A GAL fit also gave the inclination and position angle of the inner disk. However, these quantities are dependent on the non-circular rotation, which are not negligible in the central regions. Therefore, we adopted the inclination (58°) and position angle (140°) determined from optical images of the entire stellar disk.

Figure 4 shows the radial profile of the CO-line intensities in units of $\text{Jy km s}^{-1} \text{ arcsec}^{-2}$, which is corrected for the inclination. At first, low-resolution integrated-intensity map was corrected for primary-beam attenuation. We then applied the AIPS task IIRING to azimuthally average the integrated intensities in each annulus with corrections for the inclination. We applied the central positions derived above and the inclination and position angle provided from optical observations (table 1). Figure 5 displays a position–velocity diagram (P–V diagram) along the optically defined major axis (P.A. = 140°) with a slit width of $5''$ and $60''$, respectively. The velocities have not been corrected for the inclination.

2.3. Supplementary Data

We obtained optical photographs of NGC 4501 from archives for a comparison. We overlaid low-resolution CO map contours on a Digitized Sky Survey *B*-band image in order to see the global pattern (figure 6). We also overlaid high-resolution CO map contours on an unsharp-masked image made from the HST WFPC2 observations at the F606W (wide *V*-band) filter (Carollo et al. 1998), in order to see the innermost $r < 500 \text{ pc}$ region with a higher resolution (figure 7).

3. Results

The obtained CO map (figure 1) shows spiral arms and a strong central condensation. The central CO condensation is resolved into double peaks in the higher resolution map (figure 2). We describe these components in the following subsections.

3.1. Main Disk

3.1.1. Distribution in the main disk

The entire CO disk of NGC 4501 has an exponential profile of scale length $0'.7$, and it continuously extends to $r \sim 3'.8$ (Kenney, Young 1988). We now discuss the central $r \lesssim 40''$ (3.1 kpc) region of the CO main disk (figure 1, Left). The radial profile is nearly exponential (figure 4), and the emission enhancements due to the molecular spiral arms are distinct (subsection 3.2).

3.1.2. Kinematics of the main disk

The velocity field (figure 1, Right) shows rotation of the main disk with the north-west side approaching and the south-east side receding. It represents non-circular motions superposed on regular rotation of the disk. The non-circular motions appear as a distortion of the isovelocity contours. The isovelocity contours around the spiral arms of $r \sim 2.9 \text{ kpc}$ (the ellipse in figure 1) indicate that the near (northeastern) sides of the arms are receding, and the far (southwestern) sides are approaching, as compared with pure circular motions. The non-circular motions also appear in $r \lesssim 10''$ as a Z-shaped pattern of the isovelocity contours. They can be attributed to spiral arms (subsection 3.2). The channel maps show the rotation of the disk and non-circular motion along the spiral arms as well (figure 3). The map centers were set at the derived dynamical center (section 2).

Figure 8 shows the inclination-corrected rotation curve. The rotation curve was derived from the position–velocity diagram along the major axis with a slit width of $3''$ using an iteration method developed by Takamiya and Sofue (2002). This method determines a rotation curve so that it can reproduce the observed position–velocity diagram.

The rotation velocity shows a steep rise in the central $5''$ to $v \sim 200 \text{ km s}^{-1}$, and then gradually rises to $\sim 290 \text{ km s}^{-1}$ at $r \sim 35''$. This velocity is similar to the rotation velocity of the outer flat part (Nishiyama et al. 2001), but slightly exceeds the HI rotation velocity, 268 km s^{-1} , at 20% of the peak flux (Cayatte et al. 1990).

3.1.3. Mass and surface brightness of the molecular gas

The mass of the molecular gas M_{H_2} is estimated from the total CO-line flux, S_{CO} , adopting a Galactic $N_{\text{H}_2}/I_{\text{CO}}$ conversion factor, X_{CO} , and the galactic distance, D , as

$$\left(\frac{M_{\text{H}_2}}{M_\odot}\right) = 7.2 \times 10^3 \left(\frac{D}{\text{Mpc}}\right)^2 \left(\frac{S_{\text{CO}}}{\text{Jy km s}^{-1}}\right) \times \left[\frac{X_{\text{CO}}}{1.8 \times 10^{20} \text{ cm}^{-2} (\text{K km s}^{-1})^{-1}}\right]. \quad (1)$$

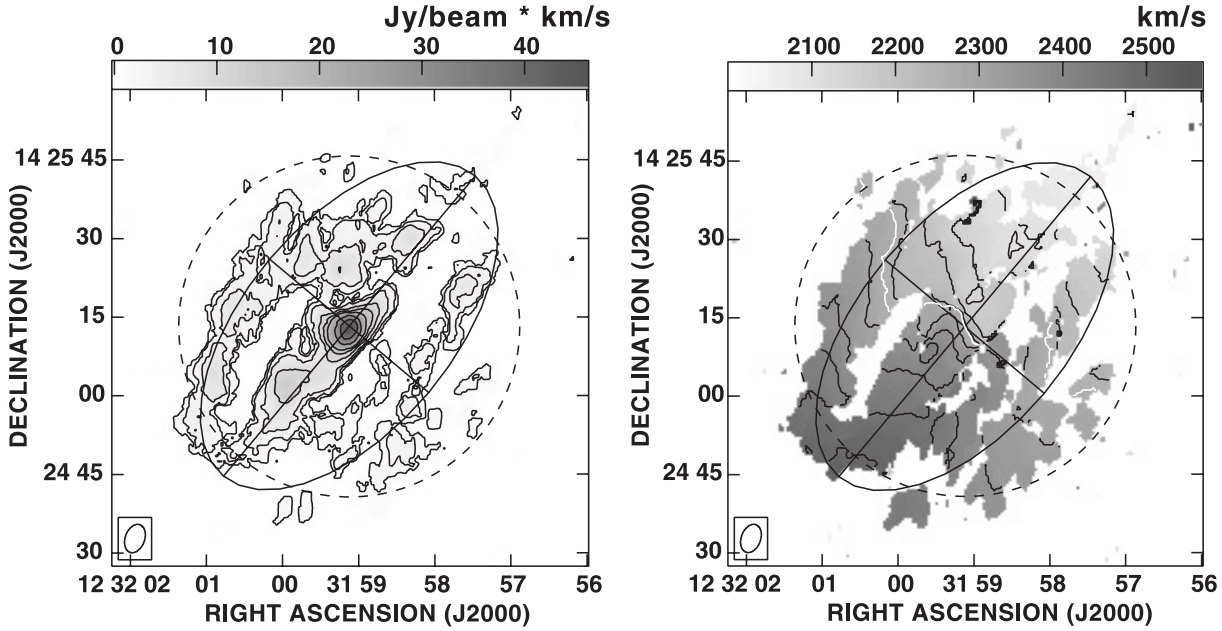


Fig. 1. Low-resolution ($5''.6 \times 3''.7$) CO (1–0) intensity map and velocity field of NGC 4501. The synthesized beam is shown in the lower left-hand corner. The primary-beam attenuation is not corrected. The clip level was 4σ ($1\sigma = 14 \text{ mJy beam}^{-1}$ in each channel) to make these moment maps. The circle represents the FWHP of NMA ($65''$). The crosses indicate the orientations of the major and minor axes of NGC 4501 (P.A. = 140°). The center of maps, crosses and ellipses are set at the dynamical center (table 2). The ellipse indicates a projected circle of a diameter of $75''$ (5.9 kpc) inclined with the position angle (140°) and the inclination (58°). Left: Intensity map in the central $90''$ (~ 7.0 kpc) squared region. The contours are drawn at 5, 10, 20, 30, 40, 60, 80% of the peak value $46 \text{ Jy beam}^{-1} \text{ km s}^{-1}$. The rms noise is $1\sigma = 1.0 \text{ Jy beam}^{-1} \text{ km s}^{-1}$. 1 Jy beam^{-1} corresponds to 4.51 K. Right: Velocity field. The contours are drawn every 50 km s^{-1} in the range of 2050–2550 km s^{-1} . The white line indicates the systemic velocity, 2261 km s^{-1} .

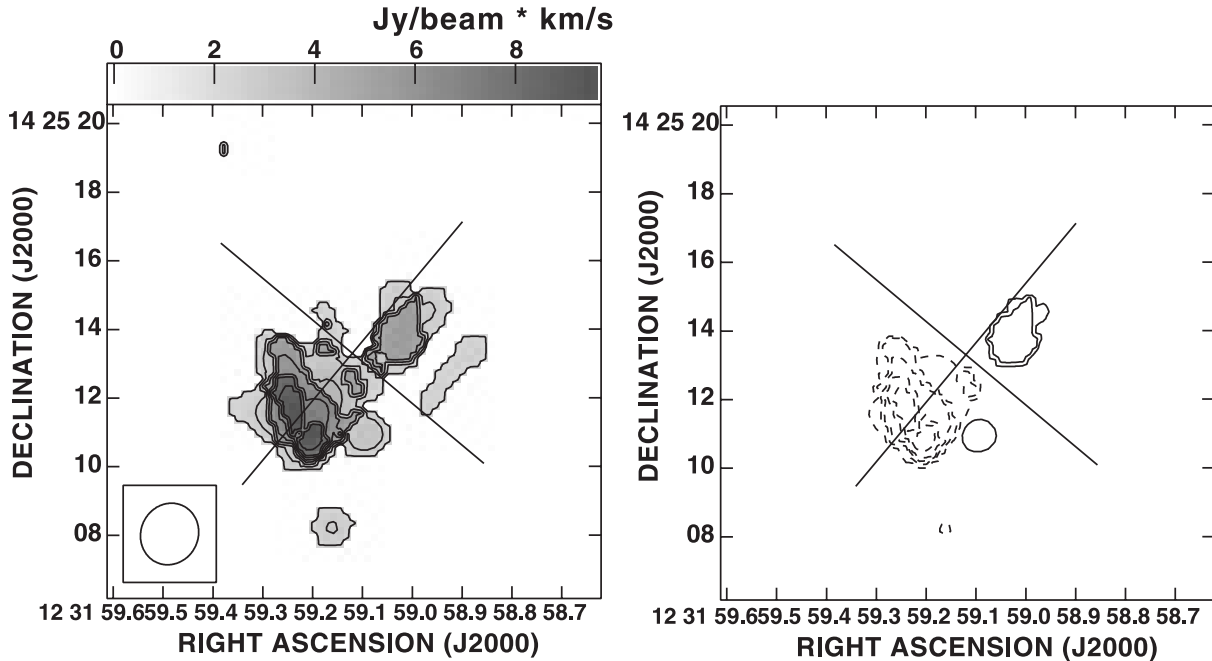


Fig. 2. High-resolution ($1''.8$) CO (1–0) intensity maps and velocity field of NGC 4501. The synthesized beam is shown in the lower left-hand corner. The primary-beam attenuation is not corrected. The clip level was 4σ ($1\sigma = 16 \text{ mJy beam}^{-1}$) to make these maps. The crosses indicate the dynamical center and the orientation of the galactic major and minor axes. Their size are $5''$ (390 pc). Left: Intensity map in the central $14''$ (~ 1.1 kpc). The contours are drawn at 30, 40, 50, 60, 70, 80, 90% of the peak value $9.6 \text{ Jy beam}^{-1} \text{ km s}^{-1}$. The rms noise is $1\sigma = 2.1 \text{ Jy beam}^{-1} \text{ km s}^{-1}$. 1 Jy beam^{-1} corresponds to 30.5 K. Right: Intensity map representing velocity field, in which approaching ($V < V_{\text{sys}}$: solid lines) and receding ($V > V_{\text{sys}}$: broken lines) components are distinguished. The contours are drawn at 30, 45, 60, 75, 90% of the peak value.

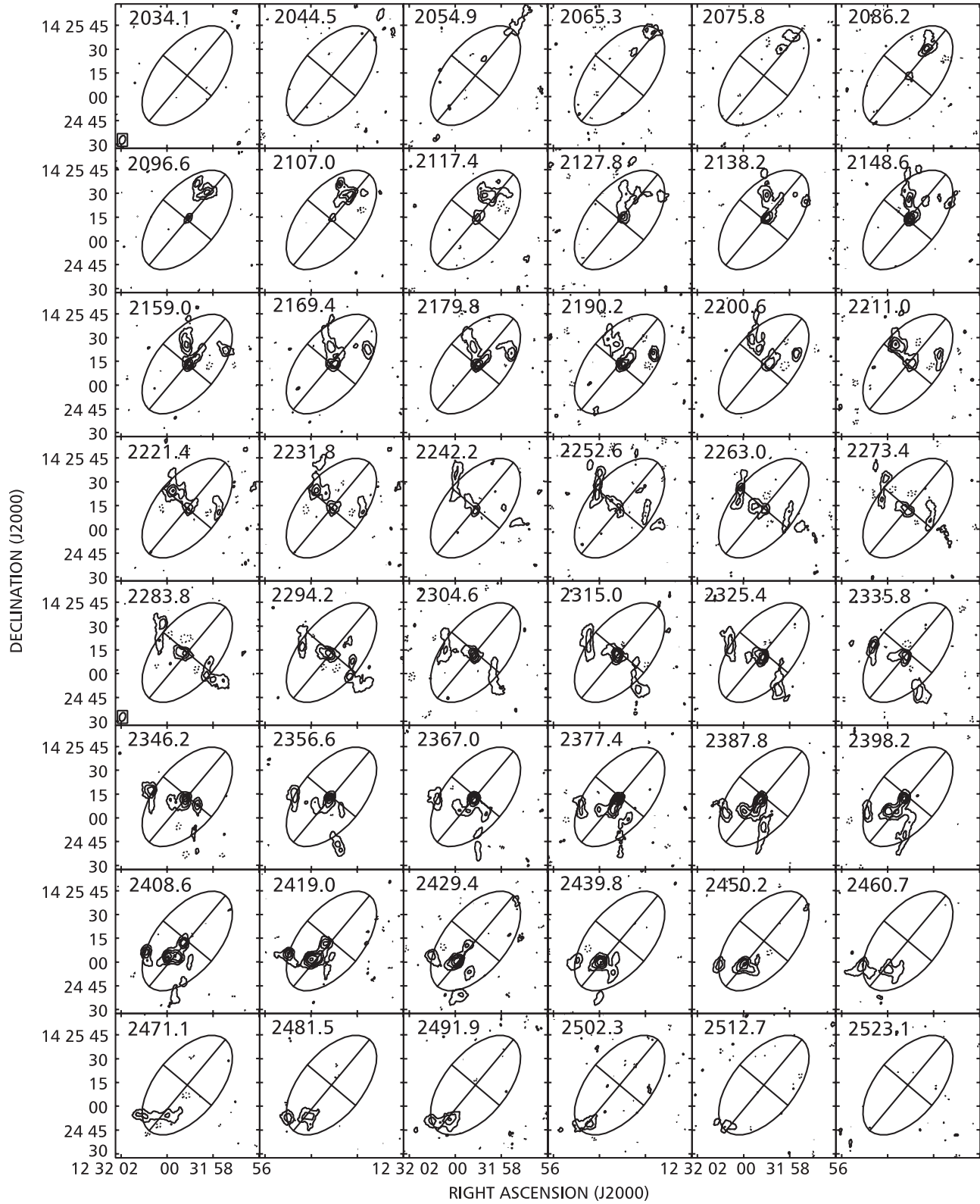


Fig. 3. Channel maps in the CO (1–0) emission. The ellipse is the same as that of figure 1. The channels have an interval of 10.4 km s^{-1} . Their central velocities (V_{LSR} in km s^{-1}) are labeled at the upper left corners. The contour levels are $-3, 3, 6, 9, 12, 15\sigma$, where $1\sigma = 14 \text{ mJy beam}^{-1}$. The negative contours are dotted. No primary-beam correction was applied. The velocity distortion along the spiral arms are apparent.

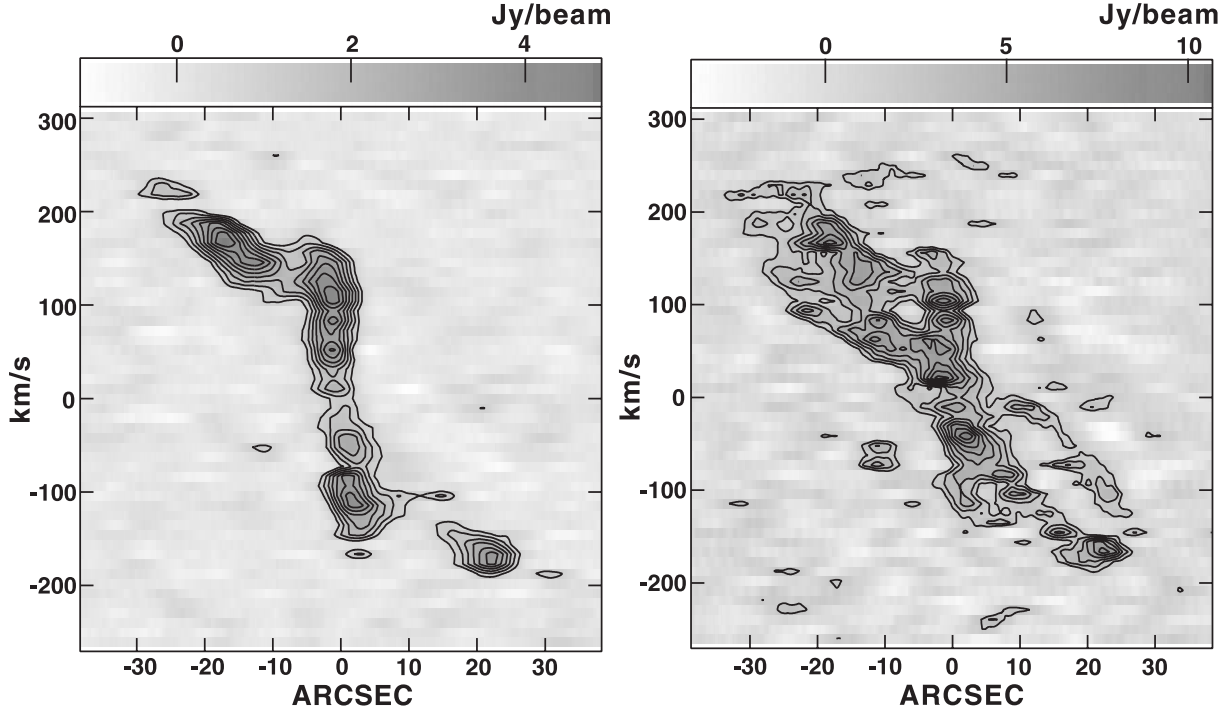


Fig. 5. Low-resolution position–velocity diagram along the major axis of NGC 4501. Velocities are not corrected for inclination (58°). Left-hand side corresponds to the northwest. Contour levels are 20, 30, 40, 50, 60, 70, 80, 90% of the peak value. Left: The slit width is central $5''$. The peak value is 4.9 Jy beam^{-1} or 51 K. The central steep rise is resolved into double peaks. Right: The slit width is $60''$, including extended spiral arms. The peak value is 11 Jy beam^{-1} or 110 K. The figure-of-eight pattern due to the spiral arms are apparent.

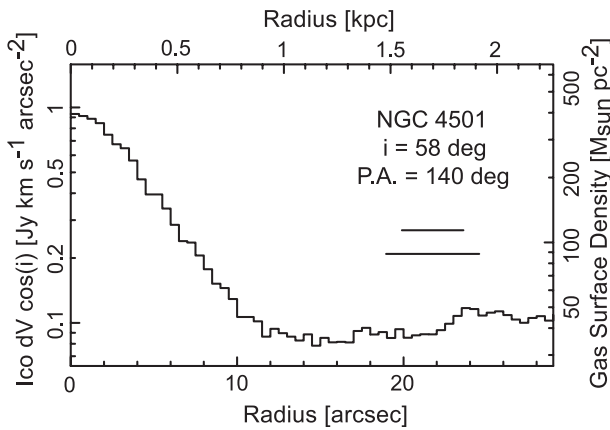


Fig. 4. Radial distribution of the molecular gas surface density in NGC 4501 with a logarithmic scale. The CO intensities were corrected for primary beam attenuation and inclination, and averaged over annuli with $0''.5 = 39.0 \text{ pc}$. $X_{\text{CO}} = 1.8 \times 10^{20} \text{ cm}^{-2} (\text{K km s}^{-1})^{-1}$ and $\Sigma_{\text{gas}} = 1.41 \Sigma_{\text{H}_2}$ was adopted to calculate the total gas surface density in unit of mass per parsec square. The two horizontal bars show the beam size along the major and minor axes ($5''.6 \times 3''.7$).

The gas surface densities are independent of the adopted distance to the galaxy. If we assume the hydrogen mass fraction 0.707 (Däppen 2000), the total gas mass including other elements, such as helium, becomes $M_{\text{gas}} = 1.41 M_{\text{H}_2}$. The surface mass density of molecular hydrogen on the galaxy plane is calculated from the integrated CO-line intensity, I_{CO} , the galaxy inclination, i , and the conversion factor, X_{CO} , as

$$\left(\frac{\Sigma_{\text{H}_2}}{M_\odot \text{ pc}^{-2}} \right) = 3.0 \times 10^2 \cos i \left(\frac{I_{\text{CO}}}{\text{Jy km s}^{-1} \text{ arcsec}^{-2}} \right) \times \left[\frac{X_{\text{CO}}}{1.8 \times 10^{20} \text{ cm}^{-2} (\text{K km s}^{-1})^{-1}} \right]. \quad (2)$$

We adopt the conversion factor of $S_{\text{CO}} \equiv N_{\text{H}_2}/I_{\text{CO}} = 1.8 \times 10^{20} \text{ cm}^{-2} (\text{K km s}^{-1})^{-1}$ (Dame et al. 2001) from observations in the Galaxy, while X_{CO} could be smaller in galactic center regions (Arimoto et al. 1996). The total flux within $r = 5 \text{ kpc}$ ($32''$) is $S_{\text{CO}} = 3.9 \times 10^2 \text{ Jy km s}^{-1}$, which corresponds to $M_{\text{gas}} = 1.0 \times 10^9 M_\odot$ for the galaxy distance $D = 16.1 \text{ Mpc}$. The dynamical mass is derived from rotation curve as $M_{\text{dyn}} = r v^2 / G$, assuming circular rotation. The ratio of the total molecular gas mass to the dynamical mass, $M_{\text{gas}}/M_{\text{dyn}}$, $4.3 \times 10^{10} M_\odot$ ($v = 270 \text{ km s}^{-1}$), is about 2.4% within $r \sim 5 \text{ kpc}$.

3.2. Spiral Arms

Two molecular spiral arms extend out from the center to the end of our field of view in the map. The arms start from the northern side and the southern side of the nucleus, and continue to the northeast arm and the southwest arm, respectively. Their outer parts are less clear owing to the primary beam attenuation. These spiral arms are distinct up to $r \sim 50''$ in larger spatial coverage, but lower resolution map by Wong and Blitz (2002). Our result shows these arms more clearly, owing to the higher resolution ($\sim 5''$). It also shows many giant molecular cloud associations in the arms. These arms are coincident with the dust lanes ($r \sim 2.9 \text{ kpc}$) in an optical image (figure 6). The dust lanes are continuous down to the nuclear

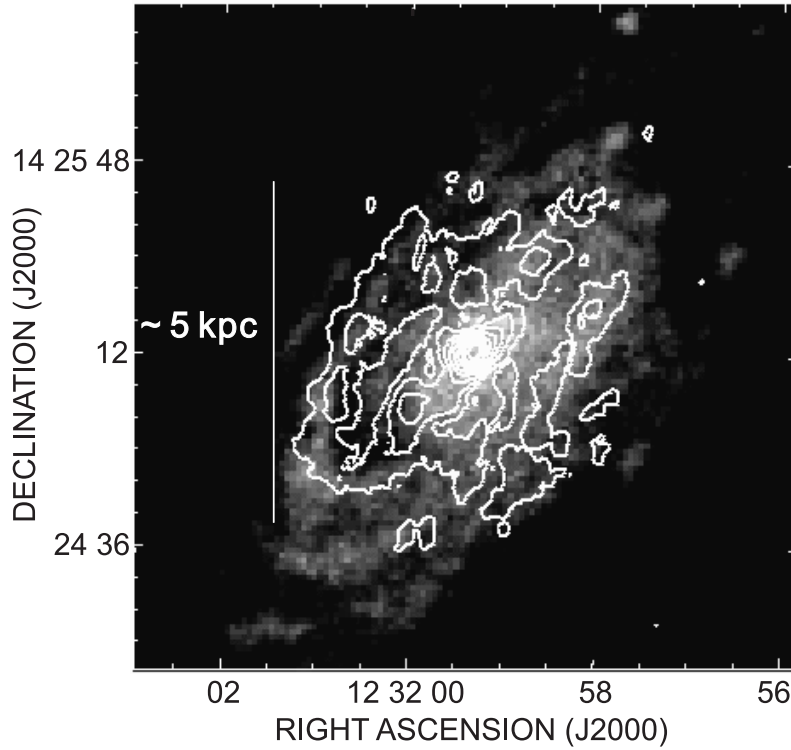


Fig. 6. Comparison of the low-resolution CO map (contours) and the *B*-band image (gray scale, from the DSS archive). Northeastern CO spiral arms trace dark dust lanes.

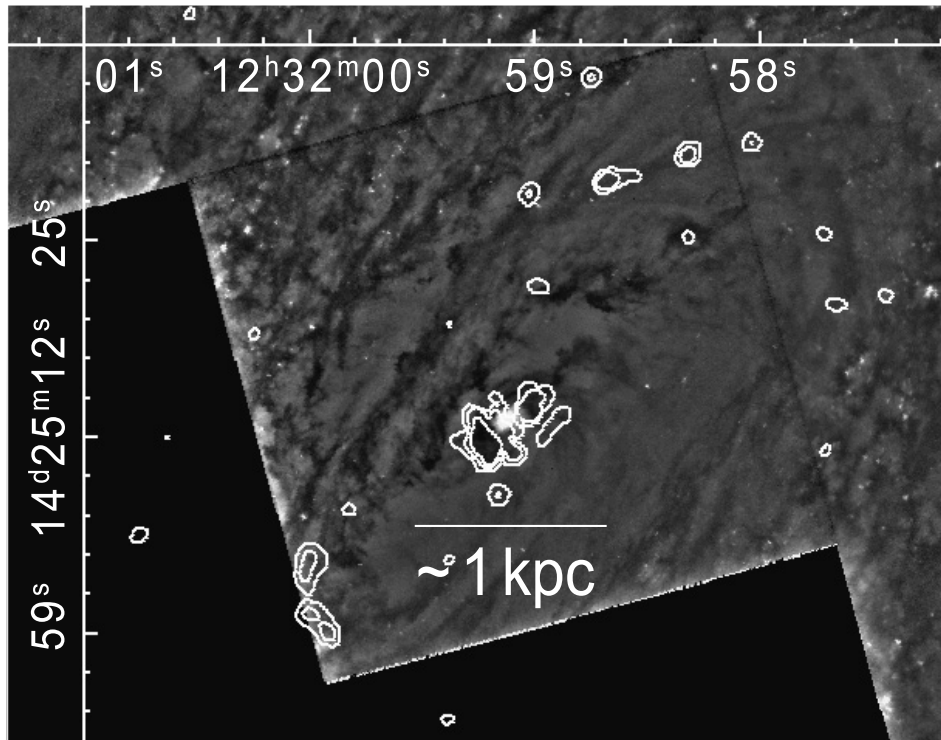


Fig. 7. Comparison of a high-resolution CO map (contours) and an unsharp-masked HST wide *V*-band image (gray scale). CO double peaks are located on the roots of spiral dust lanes.

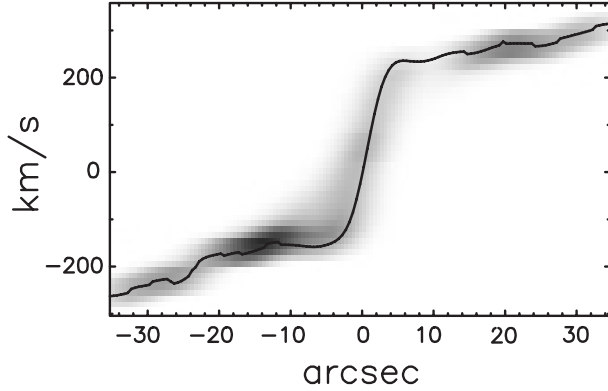


Fig. 8. Rotation curve derived by an iteration method of Takamiya and Sofue (2002) and reproduced position–velocity diagram by convolving the rotation curves with the observed intensity distribution. The velocities are corrected for inclination.

region of ~ 500 pc. The line-of-sight velocities along these arms show deviations from that of a circular-rotating disk. It is about $\sim 50 \text{ km s}^{-1}$ on the galactic minor axis. They appear in the position–velocity diagram as a “figure-of-eight” pattern (figure 5). These distortions in the velocity field is similar to that of the H I spiral arms of M 81 (Visser 1980), which are typical in gaseous spiral arms caused by density waves.

3.3. Central Double Peaks

The low-resolution map shows a central condensation of radius $\sim 5''$ (~ 390 pc). The total CO flux of this component is $S_{\text{CO}} = 48 \text{ Jy km s}^{-1}$, which corresponds to $M_{\text{gas}} = 1.3 \times 10^8 M_{\odot}$. The gas-to-dynamical mass ratio within $r = 5''$ (390 pc) is $\sim 3.5\%$, since the dynamical mass derived from $v \sim 200 \text{ km s}^{-1}$ at $r = 5''$ is $M_{\text{dyn}} = 3.6 \times 10^9 M_{\odot}$. The low-resolution ($5''$) velocity field indicates a slight non-circular motion. This nuclear component shows high velocities of $\sim \pm 200 \text{ km s}^{-1}$ in the position–velocity diagram, and is resolved into two bright peaks (figure 5) with distinct velocities.

The nuclear concentration is also resolved into double peaks in the high resolution ($\sim 2''$) intensity map, separated by $4''.7$ (~ 370 pc) (figure 2). Each of these corresponds to the double peaks in the P–V diagram. The net flux within $r \sim 5''$ is 14 Jy km s^{-1} in high resolution, while it is 48 Jy km s^{-1} in low resolution, because the higher resolution map missed the extended fluxes. The double peaks may be on more diffused components, which are unseen in our image.

The peak intensity in the high-resolution map is $9.6 \text{ Jy beam}^{-1} \text{ km s}^{-1}$ or 290 K km s^{-1} , which corresponds to $\Sigma_{\text{H}_2} = 440 M_{\odot} \text{ pc}^{-2}$ and $\Sigma_{\text{gas}} = 620 M_{\odot} \text{ pc}^{-2}$.

4. Gas Dynamics in NGC 4501

As we have shown above, the observed velocity field demonstrates distinct non-circular motions along the spiral arms. Its well-ordered pattern indicates that the density wave, rather than the stochastic process, dominates in the central region of this galaxy. Although this galaxy seems to be multiple-armed in the outer region, there is some evidence that it has two arms in the

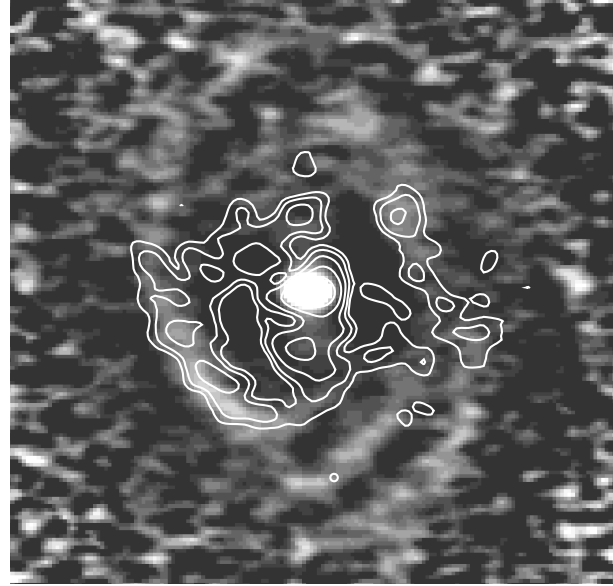


Fig. 9. Deprojected overlay of an unsharp-masked K -band image (gray: from the 2MASS archive). The vertical axis is taken to be galactic major axis.

central $r \lesssim 40''$. Elmegreen et al. (1999) showed a continuous two-armed spiral in the K' -band image, and concluded that in this galaxy there are density waves caused by the spiral arms of an older stellar population. An unsharp-masked 2MASS K -band image is shown as figure 9.

Optically unbarred galaxies sometimes unveil their hidden bars in the images at longer wavelengths (e.g., Scoville et al. 1988; Mulchaey et al. 1997; Kohno et al. 2003), because contributions from young stars and disturbances by dust lanes may make a spiral-like appearance at shorter wavelengths. Several studies have examined this galaxy for a bar, by means of elliptical isophote fitting on optical and near-infrared images (Jungwiert et al. 1997; Elmegreen et al. 1999; Sil'chenko et al. 1999). If a bar structure is dominant, the position angles and eccentricity of the isophotal ellipses are expected to vary with the radius, since the bars are triaxial and their eccentricity shows a radial variation. Near-infrared images are preferable for this purpose because of their advantage to reflect a galactic potential better than optical images. The criteria for bar identification in general is: (1) the ellipticity increases as a function of the radius, and then decreases to reveal the inclination of the disk; (2) the position angle is constant over the radii where the ellipticity is rising (McLeod, Rieke 1995; Mulchaey et al. 1997). Jungwiert et al. (1997) and Elmegreen et al. (1999) independently conducted this analysis in the H band and the K' band, respectively, and obtained quantitatively almost the same results. Interior to $r \sim 15''$, position angle remains constant at about 140° , and the ellipticity gradually rises from zero to ~ 0.4 . Then, P.A. declines to reach the minimum value of $\sim 120^\circ$ at $r \sim 27''$, and gradually recovers to attain its original value of 140° at $r \sim 50''$, and then keeps this value constantly to the outer region. The ellipticity also drops at $r \sim 20''$ to 0.3, and then gradually increases to 0.5 at $r \sim 40''$.

(see figure 4 in Jungwiert et al. and figure 5 in Elmegreen et al.)

From their quantitatively same results, Jungwiert et al. concluded that there is no evidence for a bar or other triaxiality, while Elmegreen et al. concluded the opposite. Giving a certain criteria for presence of a bar, and based on their careful simulations of the effect of projection on an identification of a bar, Jungwiert et al. concluded that the change of ellipticity in the inner region and the constancy of the P.A., as well as the fact that its value corresponds to that of the outer disk, is compatible with a spheroidal shape of the bulge. The slight change of the eccentricity and P.A. behind $r \sim 18''$ should be attributed to spiral arms. On the other hand, Elmegreen et al. noted the presence of a small bar of $15''$ diameter (see their table 1), without any explanation about the criteria to identify the bar. It seems that they might judge from the growing ellipticity in the inner region, however, as discussed in Jungwiert et al. (1997), that a bar is not relevant to explain those characteristics in this region.

Moreover, no large-scale bar has been found in NGC 4501, and the HST *V*-band image shows the spiral arms and spiral dust lanes penetrating into the nucleus (figure 7). Based on these facts, we consider the spiral structure to be prominent, rather than a bar, in the gas dynamics of NGC 4501.

In the following section, we calculate the gas cloud orbits in a potential made by stellar spiral arms by modifying the damped-orbit model of Wada (1994) to understand the gas motion in NGC 4501. Based on the spiral-arm driven gas dynamics, we suggest mechanisms of the angular-momentum transfer in spiral potentials, which could produce the central gas condensations, and probably, the double peaks.

4.1. Damped-Orbit Model in Spiral Potential

In order to study the gas responses in a weak spiral potential, we modified the damped-orbit model for a bar potential (Wada 1994). This model gives closed gas orbits in a barred potential by analytically solving the equations of motion, which include a damping-force term, to emulate the collisional nature of the gas. It has been applied to galaxies NGC 5005 (Sakamoto et al. 2000) and NGC 3079 (Koda et al. 2002), and successfully explains the observed gas motions in these barred galaxies. Instead of a straight bar potential, we used a spiral potential. Modeling after Binney and Tremaine (1987), we assume that the stellar potential is represented by an axisymmetric disk potential, Φ_0 , and a first-order perturbation owing to the spiral arms, Φ_1 , as

$$\Phi(R, \psi) = \Phi_0(R) + \Phi_1(R, \psi). \quad (3)$$

We use the Plummer potential for the axisymmetric disk part,

$$\Phi_0(R) = -\frac{1}{\sqrt{R^2 + a^2}}. \quad (4)$$

The scale length of the model is normalized by a . Φ_1 is the first-order perturbation by spiral arms, written as

$$\Phi_1(R, \psi) = \Phi_p(R) \cos[m(\Omega_0 - \Omega_p)t + p \log(R)], \quad (5)$$

which represents a logarithmic m -armed spiral with $p \equiv m \cot \theta$, where θ is the pitch angle of the spiral arms. We set $m=2$ and $\theta=17^\circ$ to represent the *K*-band feature of NGC 4501. The amplitude of the deviation from the axisymmetric part is

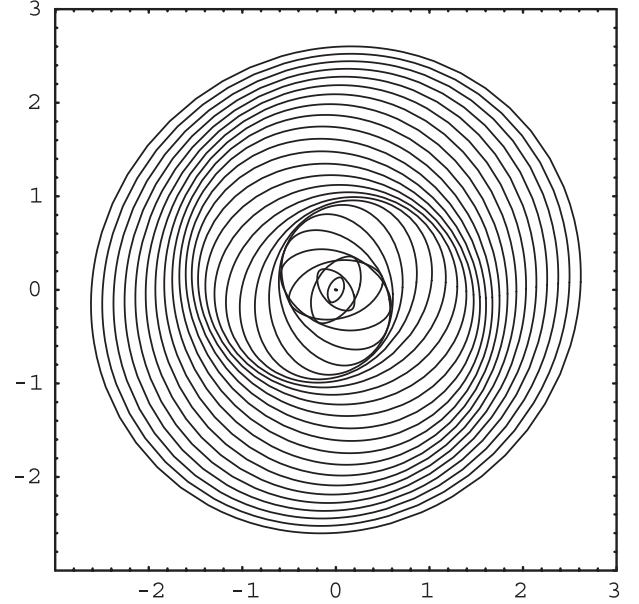


Fig. 10. Particle orbits in the fixed spiral potential. An orbit-crowding region is generated as a spiral pattern. Used parameters: $\theta = 17^\circ$, $\epsilon = 0.03$, $\Lambda \equiv \lambda/\kappa = 0.1$, $\Omega_b = 0.01$, $a = 1$.

taken to be

$$\Phi_p(R) = \epsilon \frac{aR^2}{(R^2 + a^2)^2}, \quad (6)$$

which was used for bar models by Sanders (1977) and Wada (1994). We solve the equations of motion for test gas particles moving in this potential (see appendix 1 for the detailed description for damped-orbit model in a spiral potential). The resultant orbits are shown in figure 10. Oval orbits appear, whose major axes change with the radius. As a result, spiral-shaped orbit-crowding regions are generated.

4.2. Comparison with CO Distribution and Velocity Field

Figure 11 shows the density distribution and velocity field obtained from orbit calculations. They are projected with the inclination and position angle of NGC 4501. The density distribution was simply estimated based on the assumption that the staying time of a gas cloud at each point is inversely proportional to the velocity. The observed radial profile was applied. After that, we convolved the model images with a Gaussian beam of FWHP $65''$ to reflect the primary-beam attenuation of NMA. Our model (figure 10) shows that the clouds slow down near to the major axes of the oval orbits, which make the orbit-crowding region. The cloud distribution becomes similar to the orbit-crowding pattern, and gas clouds moving in a spiral potential gather along the spiral pattern. This naturally explains the observed molecular arms. The distortions along the spiral arms and in the nuclear region of the model velocity field well represent that of the observations. The velocity field in figure 11 shows that the trends in the line-of-sight velocity of gas clouds change across the arms. On the far side of the arms to us, gas is approaching compared to circular motion. When we look nearer and nearer, its line-of-sight velocity approaches

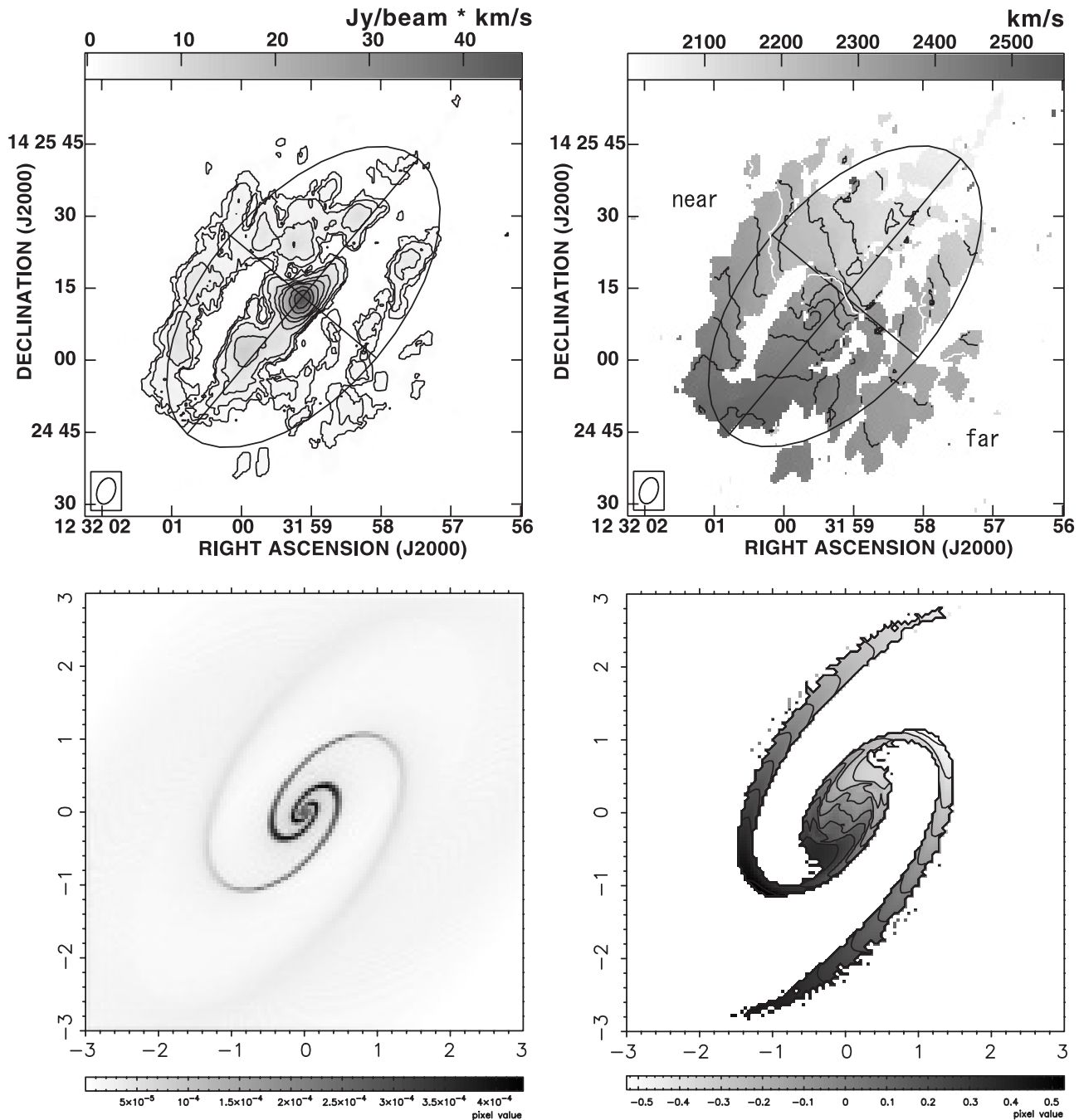


Fig. 11. Gas distributions (left panels) and velocity fields (right panels) obtained by observations (upper panels) compared to those by our models (lower panels). The parameters used for the model are the same as that used for figure 10. The model disk is inclined with the inclination and position angle of NGC 4501.

that of the circular motion. After that, it turns to receding motion, and gradually returns to the approaching motion. This behavior is well reproduced by this model.

5. Discussion

5.1. Central Double Peaks

Figure 7 shows that the double peaks inhabit the root of spiral dust lanes penetrating into the nucleus. The nuclear

spiral dust lanes have recently been found in many galaxies, and are thought to be the location of shock, and trace the sites of angular-momentum transfer, since shocks cause a loss of kinetic energy. (e.g. Regan, Mulchaey 1999; Martini et al. 2003). The CO “twin peaks” are often found in barred galaxies (e.g. Kenney et al. 1992). The “twin peaks” are connected to large-scale dust lanes, and regularly accompany to nuclear star-forming rings, and regularly accompany to nuclear star-forming rings. They show a gas-to-dynamical mass ratio of as high as ~ 0.3 , and are thought to be gravitationally unstable

enough for star formation. They are often considered to be an orbit-crowding region with an x_1/x_2 orbit population change near to the inner Lindblad resonance. On the other hand, the gas-to-dynamical mass ratio within $r = 5''$ (390 pc) is $\sim 3.5\%$ and no nuclear star-forming ring is seen near to the double peaks in NGC 4501 (see figure 5 in Koopmann et al. 2001). This is the first time that this kind of “twin peaks” was found in a non-barred galaxy, although the physical conditions are significantly different from that of the “twin peaks” in barred galaxies. An inner Lindblad resonance also exists in the spiral potential, and the appearance of double peaks might indicate that they are associated with the inner Lindblad resonance, as well as those in barred galaxies. However, it cannot be judged from our present data only, because the central rotation curves are derived from a $5''$ resolution velocity field, while the double peaks are at $r \sim 2''4$. In fact, the epicyclic frequency, $\kappa \equiv \sqrt{(d^2\Phi_0/dR^2) + 3\Omega^2}$, is sensitive even to small errors in the rotation curves. Observations at higher resolution and sensitivity still remain as future work.

5.2. Central Condensation and Mechanisms of Angular Momentum Transfer

As revealed by Sakamoto et al. (1999a), central CO condensations within $r \sim 500$ pc are prevalent in CO-luminous galaxies, and NGC 4501 is one of those with central CO excess. In terms of its radial profile, the much shorter e -folding radius ($4''3 \sim 340$ pc; this work) than that of the global CO disk ($47''0 \sim 3.8$ kpc; Nishiyama et al. 2001) evidences some distinct origins of the central gas disk from that of the global gas disk. Thus, it indicates a possible radial inflow of the gas toward the central disk.

There are two possible mechanisms to transfer angular momentum and transport the gas into the central region in a global perturbation, like bars or spirals. In the following, we consider these mechanisms in a spiral potential, and estimate the effectiveness.

- (1) *Galactic Shock Wave*: The calculation shows that the orbits are crowded along the spiral pattern. It is likely that galactic shock occurs in these orbit-crowding regions, and that this leads to the loss of angular momentum of the gas clouds. We estimated this loss by considering the oblique shock of isothermal gas. A detailed description is shown in appendix 2. The strength of the shock depends on the angle between the shock front and the gas streamline. With simple approximations, the loss of angular momentum is $\sim \sin^2\theta$ times the initial value after a shock. Adopting a pitch angle of $\theta = 17^\circ$ for NGC 4501 derived from K' -band image, the loss is estimated to be 16% after an orbital rotation.
- (2) *Drag of Stellar Spiral Potential*: Gas clouds show elliptical orbits in a nonaxisymmetric potential made by stellar spiral arms. Therefore, when a cloud is in the leading side of the potential valley, gravitational torques from the stellar spirals are exerted to drag the cloud ‘backwards’, which result in angular-momentum transfer from the gas to the stars. Note that gas clouds will oppositely obtain angular momentum when they are on the trailing side. Whether a gas cloud loses or obtains

angular momentum at a certain radius is determined by integration of this torque along the orbit of the gas, as shown in equation (A23). In a bar potential, the phase of the major axis of elliptical orbits always leads the bar potential inside of the corotation resonance (CR); therefore, clouds stay longer in the leading side of the potential valley than in the trailing side. This leads to a loss of the angular momentum and inflow of the gas inside CR (Wada 1994). We calculated the change of angular momentum, $\Delta J_z(R_0)$, for a spiral potential of $\theta = 17^\circ$, and obtained the loss of the angular momentum, $\Delta J_z(R_0)/J_z(R_0) = 0.8\%$, at most, using the parameters presented with figure 10. This value depends on spiral perturbation strength, ϵ , and pitch angle, θ .

The above estimations show that the angular-momentum variation due to galactic shock (16%) is an order-of-magnitude larger than that of gravitational torques (0.8%). Therefore, gas clouds are destined to lose angular momentum due to shocks regardless of a gain or loss due to the torques from the stellar spiral potential.

6. Conclusions

We have observed CO (1–0) emission from the non-barred Seyfert 2 galaxy NGC 4501 to study the gas dynamics in the central 5 kpc region.

1. In the central 5 kpc, NGC 4501 has two molecular gas components — spiral arms penetrating into the nuclear region, and a central concentration with radius $5''$ (~ 390 pc), and the gas mass $M_{\text{gas}} = 1.3 \times 10^8 M_\odot$.
2. The spiral arms are observed from the nuclear region to the end of our field-of-view ($r \sim 40''$). The velocity field along these arms shows deviations from circular motion. That is about $\sim 50 \text{ km s}^{-1}$ in line-of-sight velocity on the galactic minor axis.
3. The central concentration is resolved into double peaks separated by $4''7$ (~ 370 pc) in the high-resolution map. The double peaks are located on the root of nuclear dust spirals found by HST.
4. The well-ordered non-circular motion reveals that the gas is driven by density waves in the central region of this galaxy, rather than by stochastic processes. This result is consistent with that inferred from near-infrared observations.
5. To understand gas motions in NGC 4501, we studied the gas cloud orbits in spiral potential with the damped-orbit model. The result well explains the velocity field. The gas dynamics in NGC 4501 can be well understood as being governed by a spiral potential. The observed density distribution can also be explained by a simple assumption that the staying time of clouds is inversely proportional to its velocity at each point.
6. Centrally-condensed double peaks have a low star-forming efficiency, which may come from gravitational stability of gas, owing to low gas-to-dynamical mass ratio. It may be possible that they are the results of angular-momentum transfer due to shocks in nuclear dust spirals.

7. Based on our model, we estimated the loss of angular momentum in NGC 4501 due to two possible mechanisms — galactic shock in orbit-crowding regions and gravitational torques exerted by the stellar spiral potential. The effect of galactic shock is an order-of-magnitude larger than that of gravitational torques. Stellar spiral arms are responsible for the angular-momentum loss of gas, and may lead to gas inflow toward the galactic centers. The gas inflow rate depends on the galactic morphology. Our spiral model and its consequential gas inflow are natural extensions of those discussed for a bar. The spiral-shock inflow mechanism, as well as a bar-induced inflow, can be a potent instrument to study the relation between the galactic morphology and the central gas features, such as nuclear condensations and starbursts.

The authors thank an anonymous referee for comments, which refined this paper. We are indebted to the NRO staff for their support with observations. We are grateful to Hiroyuki Nakanishi and Tsutomu Takamiya for their help with observations and reductions and for useful comments. We also appreciate Keiichi Wada for his profitable comments. S. O. and J. K. are financially supported by the Japan Society for the Promotion of Science (JSPS) for Young Scientists.

Appendix 1. Gaseous Orbits in Spiral Potential

In section 4, we used the damped orbit model to describe gas motions in a spiral potential. This model follows Binney and Tremaine (1987), which described analytic solutions of equations of motion for collisionless particles in a weak bar, and obtained stellar orbits under an epicyclic approximation. Wada (1994) introduced the damping force term considering the collisional nature of gas, and obtained gas orbits in a bar potential. We modify this damped-orbit model to introduce a spiral potential, instead of a barred potential. We will consider the gas clouds moving in a fixed stellar potential. The self gravity of gas is not taken into account.

We assume that the pattern of a potential rotates with a certain pattern speed, Ω_p . Let (R, ψ) be polar coordinates in a frame that rotates with the potential, $\Phi(R, \psi)$. The equations of motion of a test particle in this frame are written as

$$\ddot{R} - R\dot{\psi}^2 = -\frac{\partial\Phi}{\partial R} + 2R\dot{\psi}\Omega_p + \Omega_p^2 R, \quad (\text{A1})$$

$$R\ddot{\psi} + 2\dot{R}\dot{\psi} = -\frac{1}{R}\frac{\partial\Phi}{\partial\psi} - 2\dot{R}\Omega_p. \quad (\text{A2})$$

Here, we derive analytic solutions of equations of motion to the first order. We assume that the non-axisymmetric part of the potential, Φ_1 , is much weaker than the axisymmetric part, Φ_0 , then

$$\Phi(R, \psi) = \Phi_0(R) + \Phi_1(R, \psi), \quad (\text{A3})$$

where $|\Phi_1/\Phi_0| \ll 1$. We divide R and ψ into zeroth- and first-order parts:

$$R(t) = R_0 + R_1(t); \quad \psi(t) = \psi_0(t) + \psi_1(t). \quad (\text{A4})$$

We then substitute these expressions into equations (A1) and (A2). Now, the first-order terms become

$$\ddot{R}_1 + \left[\frac{d^2\Phi_0}{dR^2} - \Omega^2 \right]_{R_0} R_1 - 2R_0\Omega_0\dot{\psi}_1 = - \left[\frac{\partial\Phi_1}{\partial R} \right]_{R_0}, \quad (\text{A5})$$

$$\ddot{\psi}_1 + 2\Omega_0\frac{\dot{R}_1}{R_0} = -\frac{1}{R_0^2} \left[\frac{\partial\Phi_1}{\partial\psi} \right]_{R_0}, \quad (\text{A6})$$

where

$$\Omega(R) \equiv \pm \sqrt{\frac{1}{R} \frac{d\Phi_0}{dR}}, \quad (\text{A7})$$

$$\Omega_0 \equiv \Omega(R_0); \quad \psi_0 \equiv (\Omega_0 - \Omega_p)t, \quad (\text{A8})$$

$$\kappa_0 \equiv \sqrt{\frac{d^2\Phi_0}{dR^2} + 3\Omega^2}. \quad (\text{A9})$$

We now introduce a spiral-shaped perturbation,

$$\Phi_1(R, \psi) = \Phi_p(R) \cos[m(\Omega_0 - \Omega_p)t + p \log(R)], \quad (\text{A10})$$

which represents an m -armed logarithmic spiral with $p \equiv m \cot \theta$, where θ is the pitch angle of the spiral arms. Next, we add a damping-force term to the equation of motion (A5) following Wada (1994). The damping force term represents the effects of the collisional nature of gas; thus, a plausible approximation can be the form of $2\lambda\dot{R}_1$, which is proportional to the velocity of the radial oscillation, and an appropriate value, λ .

Then, the equations of motion become

$$\ddot{R}_1 + 2\lambda\dot{R}_1 + \kappa_0^2 R_1 = f_0 \cos[m(\Omega_0 - \Omega_p)t + \alpha] + f_1 \sin[m(\Omega_0 - \Omega_p)t + \alpha], \quad (\text{A11})$$

$$\ddot{\psi}_1 + 2\Omega_0\frac{\dot{R}_1}{R_0} = - \left[\frac{\partial\Phi_p(R)}{\partial R} \right]_{R_0} \cos[m(\Omega_0 - \Omega_p)t + \alpha] + \Phi_p(R) \frac{C_1}{R_0} \sin[m(\Omega_0 - \Omega_p)t + \alpha]. \quad (\text{A12})$$

We assume the axisymmetric part of the potential, $\Phi_0(R)$ to be Plummer potential (5), and the strength of the non-axisymmetric part, $\Phi_p(R)$, to be equation (6), following Sanders (1977) and Wada (1994). When we assume the gas orbits to be closed, the solutions for these equations are

$$R_1 = \frac{1}{C_1^2 + C_2^2} \{ (C_1 f_0 - C_2 f_1) \cos[m(\Omega_0 - \Omega_p)t + \alpha] + (C_2 f_0 + C_1 f_1) \sin[m(\Omega_0 - \Omega_p)t + \alpha] \}, \quad (\text{A13})$$

$$\psi_1 = -\frac{1}{C_1^2 + C_2^2} \frac{2\Omega_0}{mR_0(\Omega_0 - \Omega_p)} \times \{ (C_1 f_0 - C_2 f_1) \sin[m(\Omega_0 - \Omega_p)t + \alpha] - (C_2 f_0 + C_1 f_1) \cos[m(\Omega_0 - \Omega_p)t + \alpha] \} - \frac{\Phi_p(R)}{mR_0^2(\Omega_0 - \Omega_p)^2} \sin[m(\Omega_0 - \Omega_p)t + \alpha], \quad (\text{A14})$$

where

$$\alpha \equiv p \log(R_0), \quad (\text{A15})$$

$$f_0 \equiv - \left[\frac{d\Phi_p}{dR} + \frac{2\Omega\Phi_p}{R(\Omega - \Omega_p)} \right]_{R_0}, \quad (\text{A16})$$

$$f_1 \equiv \Phi_p(R_0) \left[\frac{\partial \alpha(R)}{\partial R} \right]_{R_0}, \quad (\text{A17})$$

$$C_1 = \kappa_0^2 - m^2(\Omega_0 - \Omega_p)^2, \quad C_2 = 2\lambda m(\Omega_0 - \Omega_p). \quad (\text{A18})$$

Particles trace oval orbits whose position angle of the major axes changes continuously due to both the damping term and the spiral potential. This situation is different from that of stellar orbits in a bar potential, whose major axes can only be parallel or perpendicular to the bar.

Appendix 2. Estimation of Angular-Momentum Variation

A.2.1. Galactic Shocks

Behaving as a fluid, interstellar gas becomes supersonic by a variation of the local gravitational field due to the density wave (Fujimoto 1968a; Roberts 1969). This results in a galactic shock wave. It is possible that gas loses angular momentum due to galactic shocks along the spiral arms. We estimate the effect of the shock with simple approximations of isothermal gas with a Mach number of $M \gg 1$. Although the orbits are non-circular, a circular-orbit approximation is enough for an order-of-magnitude estimation. The Mach number, M , is defined as $M = v/a$ with velocity v and sound speed a . For interstellar gas, because $M \sim 10$ with $v \sim 100 \text{ km s}^{-1}$ and $a \sim 10 \text{ km s}^{-1}$, $M \gg 1$ is plausible.

We now consider the gas bumping into a shock front with velocity v_1 and angle α . In the jump condition of isothermal oblique shock, the velocity perpendicular to the shock front is reduced by $1/M^2$. It leaves then there with velocity v_2 and angle β , which are written as

$$v_2 = v_1 \sqrt{\frac{\sin^2 \alpha}{M^4} + \cos^2 \alpha}, \quad (\text{A19})$$

$$\beta = \tan^{-1} \left(\frac{\tan \alpha}{M^2} \right). \quad (\text{A20})$$

Thus the change in the angular momentum, $J_1 - J_2$, becomes

$$\begin{aligned} J_1 - J_2 &= r v_1 \cos(\theta - \alpha) - r v_2 \cos(\theta - \beta) \\ &= r v_1 \left[\cos(\theta - \alpha) - \sqrt{1 + \frac{\tan^2 \alpha}{M^4}} \right. \\ &\quad \left. \times \cos \alpha \cos \left(\theta - \tan^{-1} \frac{\tan \alpha}{M^2} \right) \right]. \end{aligned} \quad (\text{A21})$$

Then, the supersonic condition $1/M^2 \rightarrow 0$ and the circular-motion condition $\alpha \rightarrow \theta$ yield

$$J_1 - J_2 \sim \sin^2 \theta J_1. \quad (\text{A22})$$

A.2.2. Gravitational Torques

The phase difference between the major axis of the oval orbits and the potential valley results in angular-momentum transfer between the gas and the potential. The change in the angular momentum per unit time in the region R to $R + \Delta R$ and $\psi = 0-2\pi$ is calculated by integrating the torque along the orbit as

$$\Delta J_z(R_0) \equiv \int_0^{2\pi} [\mathbf{R} \times (-\nabla \Phi)]_z R \Delta R d\psi. \quad (\text{A23})$$

It was then computed numerically.

References

- Arimoto, N., Sofue, Y., & Tsujimoto, T. 1996, PASJ, 48, 275
Athanassoula, E. 1992, MNRAS, 259, 345
Binney, J., & Tremaine, S. 1987, Galactic Dynamics (Princeton, New Jersey: Princeton University Press), 146
Brandt, J. C., & Scheer, L. S. 1965, AJ, 70, 471
Carollo, C. M., Stiavelli, M., & Mack, J. 1998, AJ, 116, 68
Cayatte, V., van Gorkom, J. H., Balkowski, C., & Kotanyi, C. 1990, AJ, 100, 604
Chamaraux, P., Balkowski, C., & Gerard, E. 1980, A&A, 83, 38
Dame, T. M., Hartmann, D., & Thaddeus, P. 2001, ApJ, 547, 792
Däppen, W. 2000, in Allen's Astrophysical Quantities, 4th edition, ed. A. N. Cox (New York: Springer-Verlag), 28
de Vaucouleurs, G., de Vaucouleurs, A., Corwin, H. G., Jr., Buta, R. J., Paturel, G., & Fouqué, P. 1991, Third Reference Catalogue of Bright Galaxies (New York: Springer-Verlag) (RC3)
Elmegreen, D. M., Chromey, F. R., Bissell, B. A., & Corrado, K. 1999, AJ, 118, 2618
Elmegreen, D. M., & Elmegreen, B. G. 1987, ApJ, 314, 3
Ferrarese, L., et al. 1996, ApJ, 464, 568
Fujimoto, M. 1968a, in IAU Symp, 29, 453
Fujimoto, M. 1968b, ApJ, 152, 391
Ho, L. C., Filippenko, A. V., & Sargent, W. L. W. 1997a, ApJS, 112, 315
Ho, L. C., Filippenko, A. V., & Sargent, W. L. W. 1997b, ApJ, 487, 591
Jungwiert, B., Combes, F., & Axon, D. J. 1997, A&AS, 125, 479
Kenney, J. D. P., Wilson, C. D., Scoville, N. Z., Devereux, N. A., & Young, J. S. 1992, ApJ, 395, L79
Kenney, J. D., & Young, J. S. 1988, ApJS, 66, 261
Koda, J., Sofue, Y., Kohno, K., Nakanishi, H., Onodera, S., Okumura, S. K., & Irwin, J. A. 2002, ApJ, 573, 105
Kohno, K., Vila-Vilaró, B., Sakamoto, S., Kawabe, R., Ishizuki, S., & Matsushita, S. 2003, PASJ, 55, 103
Koopmann, R. A., Kenney, J. D. P., & Young, J. 2001, ApJS, 135, 125
Martin, P., & Roy, J.-R. 1994, ApJ, 424, 599
Martini, P., Regan, M. W., Mulchaey, J. S., & Pogge, R. W. 2003, ApJ, 589, 774
McLeod, K. K., & Rieke, G. H. 1995, ApJ, 441, 96
Mulchaey, J. S., & Regan, M. W. 1997, ApJ, 482, L135
Mulchaey, J. S., Regan, M. W., & Kundu, A. 1997, ApJS, 110, 299
Nishiyama, K., Nakai, N., & Kuno, N. 2001, PASJ, 53, 757
Okumura, S. K., et al. 2000, PASJ, 52, 393
Regan, M. W., & Mulchaey, J. S. 1999, AJ, 117, 2676
Roberts, W. W. 1969, ApJ, 158, 123
Sakamoto, K., Baker, A. J., & Scoville, N. Z. 2000, ApJ, 533, 149
Sakamoto, K., Okumura, S. K., Ishizuki, S., & Scoville, N. Z. 1999a, ApJS, 124, 403
Sakamoto, K., Okumura, S. K., Ishizuki, S., & Scoville, N. Z. 1999b, ApJ, 525, 691
Sanders, R. H. 1977, ApJ, 217, 916
Scoville, N. Z., Matthews, K., Carico, D. P., & Sanders, D. B. 1988, ApJ, 327, L61

- Shlosman, I., Frank, J., & Begelman, M. C. 1989, *Nature*, 338, 45
- Sil'chenko, O. K., Burenkov, A. N., & Vlasyuk, V. V. 1999, *AJ*, 117, 826
- Simkin, S. M., Su, H. J., & Schwarz, M. P. 1980, *ApJ*, 237, 404
- Sofue, Y., Koda, J., Nakanishi, H., Onodera, S., Kohno, K., Tomita, A., & Okumura, S. K. 2003, *PASJ*, 55, 17
- Stark, A. A., Knapp, G. R., Bally, J., Wilson, R. W., Penzias, A. A., & Rowe, H. E. 1986, *ApJ*, 310, 660
- Takamiya, T., & Sofue, Y. 2002, *ApJ*, 576, L15
- Tsutsumi, T., Morita, K.-I., & Umeyama, S. 1997, in *ASP Conf. Ser. 125: Astronomical Data Analysis Software and Systems VI*, ed. G. Hunt & H. E. Payne, 50
- Visser, H. C. D. 1980, *A&A*, 88, 149
- Wada, K. 1994, *PASJ*, 46, 165
- Wong, T., & Blitz, L. 2002, *ApJ*, 569, 157